ORIENTAL JOURNAL OF CHEMISTRY
An International Open Access, Peer Reviewed Research Journal
www.orientjchem.org
ISSN: 0970-020 X
CODEN: OJCHEG
2026, Vol. 42, No.(5):
Pg. 1846-1869

Integrated Molecular Docking and Density Functional Theory Studies of a Polyhydroxylated Chromen-4-one Flavonoid (5H3M1P1C4O) Against Multiple Protein Targets

THANGAVELAN NIRUBAN BALU[1]*, P. VENKATESH[2] and RAJAKUMARI SUBRAMANIYAN[3]

*[1]Department of Chemistry, Velammal Engineering College, Chennai, Tamil Nadu, India
[2]Department of Chemistry, Pachaiyappa's college, Chennai, Tamil Nadu, India
[3]Assistant Professor (SG),Department of Chemistry,Rajalakshmi Engineering College (REC) Thandalam, Chennai, Tamil Nadu, India
*Corresponding author E-mail : niruban.t@gmail.com

http://dx.doi.org/10.13005/ojc/420508

(Received: March 16, 2026; Accepted: April 25, 2026)

ABSTRACT

5H3M1P1C4O, a polyhydroxylated chromen-4-one flavonoid (2-3,4-dihydroxy-5,7-dihydroxy-3,4,5-trihydroxy-6-hydroxymethoxy-chromen-4-one), was studied in relation to four protein targets: 3ERT, 6J90, 7RPU, and 8TSK. The combined computational approach utilized molecular docking and density functional theory (DFT) calculations. All targets showed energetically favorable ligand-protein complex formation in the molecular docking study, with negative binding energy values; comparative examination showed that different proteins had different binding affinities and contact distances. The best binding profile, indicating better ligand accommodation and improved non-covalent stabilization, was seen in 7RPU, out of all the systems that were investigated. 5H3M1P1C4O exhibited excellent chemical stability and appropriate reactivity for molecular recognition, as revealed by DFT calculations conducted at the B3LYP/6-311++G(d,p) level, which supplemented the docking results by shedding light on the electronic structure, charge distribution, and frontier molecular orbital features of the compound. This compound has great promise as a scaffold for future research into the structure-activity connection as well as experimental validation, thanks to the mechanistic insights provided by the combined docking and DFT results regarding the structure-interaction relationship of 5H3M1P1C4O across several protein targets.

Keywords: Molecular Docking, Quantum Chemical Analysis; Computational Drug Discovery.

INTRODUCTION

Cancer remains a major global health burden, with breast, lung, colorectal, pancreatic, and prostate accounting for a substantial proportion of worldwide cancer incidence and mortality[1-2]. These malignancies are characterized by pronounced molecular heterogeneity, complex signaling dysregulation, and high adaptive potential, which collectively contribute to tumor progression,

This is an Open Access article licensed under a Creative Commons license: Attribution 4.0 International (CC- BY).
Published by Oriental Scientific Publishing Company © 2018

metastasis, and therapeutic resistance[3-5]. Despite significant advances in cancer diagnosisand treatment, lung and pancreatic cancers continue to exhibit poor clinical outcomes, while breast, colorectal, and prostate cancers frequently develop resistance during prolonged therapeutic regimens. Moreover, the limited selectivity and systemic toxicity associated with many currently used anticancer agents restrict their long-term efficacy and patient compliance. Accordingly, the development of novel anticancer compounds with improved potency, selectivity, and safety profiles remains a central challenge in modern medicinal chemistry[6-7].

In response to the limitations of conventional anticancer drug discovery, modern medicinal chemistry increasingly relies on computational approaches that enable the rational investigation of bioactive compounds at the molecular level. Among these, structure-based molecular docking and density functional theory (DFT) calculations represent complementary and widely accepted tools for elucidating ligand–target interactionsand intrinsic electronic properties relevant to biological activity[8-10]. Molecular docking provides structural insight into binding modes, key intermolecular interactions, and relative binding affinities of small molecules toward cancer-associated protein targets, thereby supporting lead identification and optimization. In parallel, DFT calculations offer a detailed understanding of electronic structure, molecular reactivity, and stability, which are critical determinants of target recognition and binding behaviour[10-12]. For the purpose of accurately assessing the global reactivity descriptors and frontier molecular orbitals of biologically active chemicals, the B3LYP functional in conjunction with the 6-311++G(d,p) basis set has seen considerable application. To rationally explore possible anticancer drugs before experimental validation, a computational approach that combines molecular docking with high-level DFT simulations utilizing Autodock Tools 1.5.7 is a strong and cost-effective option[8,9,13].

MATERIALS AND METHODS

Identification of the target protein

The three-dimensional crystal structures of cancer-associated proteins were retrieved from the Protein Data Bank (PDB) using the PDB IDs 3ERT, 6J90, 7RPU, and 8TSK were employed for the molecular docking analysis. A version of Autodock Tools, 1.5.7, was used for the docking analysis. All ions, water molecules, and co-crystallized ligands were removed before docking. Then, Kollman charges were applied, and polar hydrogen atoms were introduced. The PDBQT format was used to preserve the generated protein structure for future molecular docking investigations.

Ligand Retrieval and Optimization

The molecular structure of 5H3M1P1C4O was retrieved from a public chemical database and used for computational studies. The compound was procured commercially. The ligand geometry was optimized to obtain a minimum-energy conformation prior to docking analysis. Autodock tool was used to assign Gasteiger charges, define rotatable bonds, and save the ligand in PDBQT format.

Molecular docking protocol

Molecular docking simulations were carried out using the Autodock suite implemented with the Lamarckian genetic algorithm. The docking grid box was defined to encompass the active binding sites of 3ERT, 6J90, 7RPU, and 8TSK with dimensions sufficient to allow full ligand flexibility within the binding pocket. Default Autodock parameters were employed unless otherwise specified. Multiple docking runs were performed to generate diverse binding conformations. The resulting docked poses were ranked based on predicted binding energy, and the most energetically favourable conformation was selected for detailed interaction analysis using molecular visualization tools.

Density functional theory calculations

The electronic structure and reactivity characteristics of 5H3M1P1C4O were investigated by density functional theory (DFT) computations. Using the 6-311++G(d,p) basis set and the B3LYP exchange-correlation functional, geometry optimization was performed. The gas phase was used for all computations, and no symmetry restrictions were used. Calculations were made for the energies of the frontier molecular orbitals, which include the HOMO and LUMO, and the HOMO- LUMO energy gap was assessed. In order to better understand the molecular docking data, global reactivity descriptors were generated to provide light on the chemical stability and interaction potential of 5H3M1P1C4O.

RESULTS AND DISCUSSION

Molecular geometric parameters

The optimized molecular geometry of 5H3M1P1C4O was obtained using density functional theory at the B3LYP/6-311++G(d,p) level. The calculated bond lengths and bond angles are presented in Fig. 1 and Table 1. The molecule consists of carbon, oxygen and hydrogen atoms forming a stable network of C – C, C – O, and C – H bonds. The C – C bond lengths of 5H3M1P1C4O range from 1.367 to 1.534 Å. Longer bonds such as C13 – C14 (1.534 Å), C14 – C16 (1.532 Å), and C15 – C17 (1.532 Å) correspond to single-bond character within the molecular skeleton, while shorter bonds including C19 – C20 (1.367 Å) and C23 – C26 (1.389 Å) indicate partial double-bond character and conjugation, contributing to molecular rigidity. The C – O bond distances vary between 1.246 and 1.437 Å. The shortest bond, O8 – C21 (1.246 Å), suggests strong bonding interaction, whereas longer bonds such as O1 – C16 (1.437 Å) and O3 – C13 (1.425 Å) are characteristic of single C – O linkages. O – H bond lengths lie in the range of 0.963–0.990 Å, confirming the presence of hydroxyl groups capable of hydrogen bonding. Extended O – H distances observed for O3 – H42 (2.231 Å) and O12 – H52 (2.161 Å) indicate intramolecular hydrogen-bond formation. C – H bond lengths were found between 1.079 and 1.101 Å, with the shortest values corresponding to C28 – H47 (1.079 Å) and C27 – H46 (1.081 Å), supporting the structural stability of the optimized geometry. Bond angle analysis shows values consistent with ideal tetrahedral and trigonal planar geometries. The largest bond angle, H53 – O12 – H52 (166.3°)

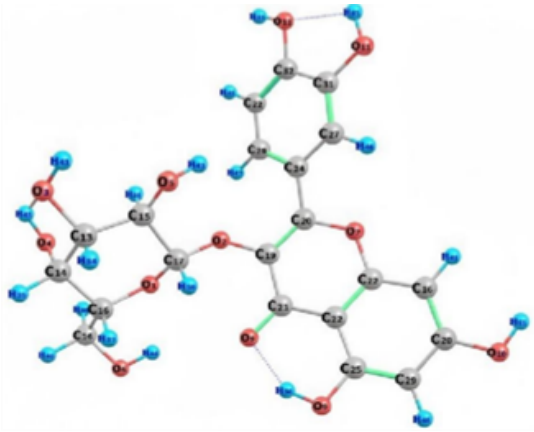


Fig. 1: Optimized molecular structure of 5H3M1P1C4O

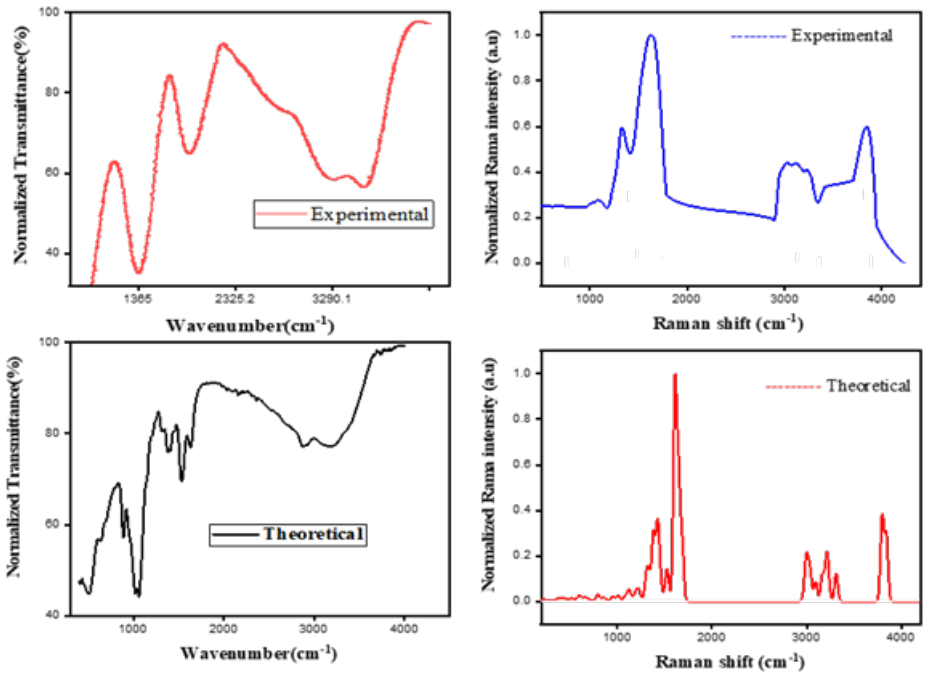


Fig. 2: FT-IR spectra and FT-Raman spectra of 5H3M1P1C4O

Table 1: Theoretical values of bond lengths and angles for the title compound 5H3M1P1C4O. (Å: angstrom unit, °:degree.)

Bond Length (Å)	DFTB3 LY P/6–311++ G (d,p)	Bond Length (Å)	DFTB3 LY P/6–311++ G (d,p)	Bond Angle (Å)	DFTB3 LY P/6–311++ G (d,p)	Bond Angle (Å)	DFTB 3L YP/ 6–311 ++G (d,p)	Bond Angle (Å)	DFTB3 LY P/6–311++ G (d,p)	Bond Angle (Å)	DFTB 3L YP/ 6–311 ++Gd,p)
O1-C16	1.437	C16-C18	1.522	C16-O1-C17	113	O6-C18-H40	106.8	C13-C15-C17	109.2	C 3 0 - C 2 6 -	122.2
O1-C17	1.4	C16-H37	1.101	O1-C16-O4	111.6	C23-O7-C20	121.8	C13-C15-H36	109.3	C 2 6 - C 3 0 -	121.9
O2-C17	1.424	C17-H38	1.097	O1-C16-C18	105.4	O7-C23-C22	120.4	C16-C14-H35	108.2	H 4 6 - C 2 7 -	118.3
O2-C19	1.37	C18-H39	1.095	O1-C16-H37	108.5	O7-C23-C26	116.9	C14-C16-C18	114.8	C 2 7 - C 3 1 -	119.6
O3-C13	1.425	C18-H40	1.092	O1-C17-O2	107.1	O7-C20-C19	121	C14-C16-H37	108	H 4 7 - C 2 8 -	119.6
O3-H41	0.965	C19-C21	1.462	O1-C17-C15	108.8	O7-C20-C24	111.5	C17-C15-H36	107.6	C 2 8 - C 3 2 -	120.4
O4-C14	1.42	C19-C20	1.367	O1-C17-H38	111.4	O8-C21-C19	122.2	C15-C17-H38	111.2	C 2 8 - C 3 2 -	119.8
O4-H42	0.966	C20-C24	1.472	C17-O2-C19	119.1	O8-C21-C22	122.4	C18-C16-H37	108.3	C 3 0 - C 2 9 -	120.2
O5-C15	1.425	C21-C22	1.448	O2-C17-C15	108.2	C21-O8-H50	100.2	C16-C18-H39	109	C 3 1 - C 3 3 -	120.1
O5-H43	0.965	C22-C23	1.4	O2-C17-H38	110	H50-O9-C25	107.3	C16-C18-H40	109.8	C 3 3 - C 3 2 -	119.8
O6-C18	1.42	C22-C25	1.427	O2-C19-C21	120.2	O9-H50-O8	148	H39-C18-H40	108.5		
O6-H44	0.966	C23-C26	1.389	O2-C19-C20	118.6	O9-C25-C22	120.5	C21-C19-C20	121		
O7-C23	1.364	C24-C28	1.404	C13-O3-H41	107.5	O9-C25-C29	119.4	C19-C21-C22	115.4		
O7-C20	1.364	C24-C27	1.406	O3-C13-C14	107.6	C30-O10-H51	110.2	C19-C20-C24	127.5		
O8-C21	1.246	C25-C29	1.388	O3-C13-C15	111.4	O10-C30-C26	121.7	C20-C24-C28	122.2		
O9-H50	0.99	C26-C30	1.397	O3-C13-H34	109.7	O10-C30-C29	116.4	C20-C24-C27	118.8		
O9-C25	1.338	C26-H45	1.083	C13-O3-H42	81.9	C31-O11-H52	108.8	C21-C22-C23	120.4		
O10-C30	1.36	C27-H46	1.081	H41-O3-H42	142.2	O11-C31-C27	119.6	C21-C22-C25	121.6		
O10-H51	0.963	C27-C31	1.385	C14-O4-H42	106.8	O11-C31-C33	120.8	C23-C22-C25	118		
O11-C31	1.36	C28-H47	1.079	O4-C14-C13	111	O11-H52-O12	112.5	C22-C23-C26	122.7		
O11-H52	0.966	C28-C32	1.393	O4-C14-C16	109.9	C33-O12-H53	111	C22-C25-C29	120.1		
O12-C33	1.371	C29-C30	1.398	O4-C14-H35	110	O12-C33-C31	115.2	C23-C26-C30	117.7		
O12-H53	0.963	C29-H48	1.082	O4-H42-O3	111.2	O12-C33-C32	124.7	C23-C26-H45	120.1		
C13-C14	1.534	C31-C33	1.404	C15-O5-H43	108.6	C33-O12-H52	82.7	C28-C24-C27	119		
C13-C15	1.527	C32-C33	1.389	O5-C15-C13	106.8	H53-O12-H52	166.3	C24-C28-H47	120.3		
C13-H34	1.099	C32-H49	1.086	O5-C15-C17	112.8	C14-C13-C15	111	C24-C28-C32	120.1		
C14-C16	1.532	O3-H42	2.231	O5-C15-H36	111	C14-C13-H34	108.8	C24-C27-H46	120.9		
C14-H35	1.1	O8-H50	1.718	C18-O6-H44	107.3	C13-C14-C16	109.3	C24-C27-C31	120.8		
C15-C17	1.532	O12-H52	2.161	O6-C18-C16	111	C13-C14-H35	108.3	C25-C29-C30	119.7		
C15-H36	1.095			O6-C18-H39	111.6	C15-C13-H34	108.3	C25-C29-H48	120.2		

Table 2: Vibrational frequency analysis of 5H3M1P1C4O: Experimental and computational comparison

Vibrational Modes	Experimental Frequency (cm-1)		Frequency (cm^{-1})		Infrared intensity		Raman intensity		PED Contribution (%)
	FT-IR	FT- RAMAN	Unscaled	Scaled	Relative	Absolute	Relative	Absolute	
153	3350	3425	3843.71	3693.81	138.629	23.781	234.481	22.3105	νOH 100
152	3325	3380	3830.4	3681.01	90.7565	15.5688	150.541	14.3237	νOH 100
151	3300	3320	3806.92	3658.45	47.02	8.06605	53.7717	5.11629	νOH 100
150	3250	3210	3796.8	3648.72	126.595	21.7168	167.975	15.9825	νOH 98
149	3200	3082	3792.45	3644.54	63.9077	10.9631	70.032	6.66343	νOH 99
148	3085	2935	3791.26	3643.4	169.354	29.0518	129.138	12.2873	νOH 98
147	3055	2865	3789.89	3642.08	57.1405	9.80217	54.9198	5.22553	νOH 98
146	3020	1662	3309.7	3180.62	461.023	79.0862	150.878	14.3558	νOH 99
145	2950	1655	3233.97	3107.85	1.9755	0.33889	33.4572	3.1834	νCH 99
144	2935	1610	3216.32	3090.88	1.244	0.2134	44.0889	4.19498	νCH 100
143	2925	1582	3215.09	3089.7	0.1517	0.02602	177.795	16.9169	νCH 99
142	2875	1462	3190.75	3066.31	1.6626	0.28521	79.7887	7.59176	νCH 100
141	2860	1270	3161.32	3038.03	12.6209	2.16505	125.892	11.9784	νCH 99
140	2850	1220	3092.82	2972.2	27.7932	4.76779	106.962	10.1773	νCH 79
139	1660	1172	3048.06	2929.19	26.5176	4.54896	13.3714	1.27227	νCH 88
138	1645	1115	3038.46	2919.96	30.6548	5.25868	106.142	10.0992	νCH 88
137	1630	1088	3019.81	2902.04	18.5548	3.18298	88.8552	8.45442	νCH 89
136	1580	1058	2998.57	2881.63	53.6082	9.19622	167.686	15.955	νCH 46
135	1490	1012	2983.36	2867.01	22.0902	3.78947	60.1473	5.72291	νCH 46
134	1465	855	2975.91	2859.85	3.1301	0.53695	26.4099	2.51286	νCH 46
133	1455	835	1687.26	1621.46	582.937	100	284.171	27.0384	νCC 22 + νHOC12
132	1445	778	1653.64	1589.15	6.1532	1.05555	432.381	41.1403	νCC 36
131	1260	765	1637.04	1573.2	181.563	31.1462	279.56	26.5997	νCC 18
130	1210	702	1634.71	1570.96	371.065	63.6544	43.2958	4.11952	νCC 18 + νOC53
129	1175	615	1624.05	1560.71	187.909	32.2348	129.582	12.3295	νCC 14
128	1160	590	1607.37	1544.68	76.6864	13.1552	1050.99	100	νCC 40
127	1150	545	1545.95	1485.66	160.713	27.5695	26.194	2.49231	νHCC19
126	1120	520	1524.56	1465.1	239.1	41.0165	160.648	15.2854	νCC 12 + νHCC14
125	1110	495	1501.15	1442.61	1.7228	0.29554	6.9368	0.66002	νCC 12 + νHCH91
124	1100	470	1490.24	1432.12	178.735	30.6611	14.3844	1.36865	νOC 14 + νHCC12 + νCCO11
123	1090	445	1482.18	1424.37	1.1875	0.20371	3.7953	0.36112	νOC 14
122	1080	420	1451.1	1394.51	77.5271	13.2994	122.839	11.6879	νCC 13
121	1070	395	1437.79	1381.72	8.3109	1.42569	12.026	1.14425	νCC 13 + νHCCC13
120	1050	370	1431.67	1375.83	60.7296	10.4179	47.7764	4.54584	νCC 13
119	1015	345	1425.91	1370.3	6.2727	1.07605	36.3617	3.45975	νHCO18
118	1008	320	1424.31	1368.76	83.1424	14.2627	292.676	27.8476	νHCO18
117	1000	295	1417.64	1362.35	26.1296	4.4824	14.16	1.3473	νHCO18

116	860	270	1402.96	1348.24	18.9522	3.25116	2.5757	0.24507	\HCO13 + \CCCH13
115	845	245	1401.34	1346.69	49.9321	8.56561	3.1578	0.30046	\HCO42 +HCOC10
114	830	220	1384.19	1330.21	212.877	36.518	229.694	21.855	\CC12
113	780	195	1383	1329.06	111.93	19.201	109.348	10.4042	\HOC14 + HCOC11
112	770	170	1369.07	1315.68	22.7689	3.90589	21.261	2.02295	\HCO13
111	760	145	1368.44	1315.07	5.4554	0.93585	5.008	0.4765	\HCO13
110	705	120	1359.89	1306.85	22.2668	3.81976	4.0052	0.38109	\HCO13
109	690	95	1344.29	1291.86	17.6131	3.02144	59.0526	5.61875	\HCO13
108	670	70	1342.48	1290.12	14.8853	2.5535	2.44	0.23216	\HCO13
107	650	< 50	1337.22	1285.07	312.862	53.6699	57.5778	5.47843	\HCO13
106	620		1313.31	1262.09	182.665	31.3352	141.79	13.491	\HCO13
105	600		1300.97	1250.23	14.4749	2.4831	2.9725	0.28283	\OC17
104	580		1288.5	1238.25	131.442	22.5482	22.7504	2.16466	\OC17
103	560		1283.76	1233.69	38.9795	6.68674	1.5464	0.14714	\OC17
102	540		1264.28	1214.97	51.8942	8.9022	1.9889	0.18924	\HOC23
101	< 520		1262.14	1212.92	1.9315	0.33134	0.7894	0.07511	\HOC23
100			1244.11	1195.59	93.5225	16.0433	2.6543	0.25255	\HOC23
99			1241.44	1193.02	203.329	34.8801	6.1869	0.58867	\HOC23
98			1231.94	1183.89	14.6346	2.51049	4.7406	0.45106	\HOC23
97			1222.24	1174.57	338.645	58.093	45.1228	4.29336	\OC14
96			1215.96	1168.54	125.082	21.4572	7.6617	0.729	\OC14
95			1209.93	1162.74	55.3913	9.50211	1.7006	0.16181	\OC12
94			1197.18	1150.49	13.89	2.38276	26.287	2.50116	\OC12
93			1177.4	1131.48	25.1413	4.31287	15.1186	1.43851	\HOC32
92			1172.04	1126.33	220.353	37.8005	2.6172	0.24902	\HOC32
91			1158.2	1113.03	56.5365	9.69856	3.955	0.37631	\HOC32
90			1142.43	1097.88	31.103	5.33557	3.0025	0.28568	\HOC32
89			1131.16	1087.04	220.819	37.8805	12.1282	1.15398	\OC16
88			1128.41	1084.4	103.982	17.8375	30.8338	2.93378	\OC16
87			1124.57	1080.71	21.1753	3.63252	3.0481	0.29002	\OC16
86			1110.26	1066.96	26.8048	4.59823	20.5222	1.95265	\OC16
85			1099.05	1056.19	248.247	42.5855	4.1409	0.394	\CC10
84			1098.51	1055.67	78.7664	13.512	5.9123	0.56255	\CC10
83			1082.73	1040.5	63.0776	10.8207	9.8217	0.93452	\CCC10
82			1072.84	1031	165.164	28.333	6.2352	0.59327	\CCC10
81			1066.72	1025.12	90.0196	15.4424	4.108	0.39087	\CCC10
80			1031.15	990.935	58.0001	9.94963	2.5077	0.2386	\OC12
79			1026.5	986.467	31.8523	5.46411	2.3388	0.22253	\OC14
78			1008.9	969.553	60.4349	10.3673	22.5392	2.14457	\CC12
77			1002.08	962.999	86.1077	14.7714	8.0169	0.76279	\CC12
76			957.39	920.052	25.1537	4.31499	13.5852	1.29261	\HCCC48
75			954.3	917.082	5.1818	0.88891	7.4196	0.70596	\HCCC48
74			941.15	904.445	21.5137	3.69057	6.3467	0.60388	\CC16
73			902.04	866.86	19.5451	3.35287	3.7866	0.36029	\HCCC74
72			889.7	855.002	24.2434	4.15884	2.7671	0.26328	\CCCO10
71			871.91	837.906	22.8617	3.92181	4.1713	0.39689	\CCCO10
70			857.62	824.173	0.5679	0.09742	0.2187	0.02081	\HOCC26 + \HCCC43

69	853.51	820.223	8.1174	1.3925	16.6594	1.58511	\HOCC26 + \HCCC43
68	833.91	801.388	104.517	17.9294	0.5622	0.05349	\OCCC10
67	822.59	790.509	30.4207	5.21852	4.4014	0.41879	\OCCC10
66	796.14	765.091	44.7337	7.67385	34.236	3.2575	\CC34
65	791.65	760.776	32.525	5.5795	0.3828	0.03642	\OCCC17
64	785.67	755.029	23.6002	4.0485	1.1739	0.11169	\OCCC13
63	782.87	752.338	8.8716	1.52188	1.3199	0.12559	\OCCC13
62	734.14	705.509	4.9567	0.8503	3.5529	0.33805	\CCCC10
61	717.85	689.854	4.6134	0.79141	0.6591	0.06271	\CCO10
60	709.68	682.002	14.006	2.40266	4.0864	0.38881	\OCCC14
59	695.16	668.049	53.5878	9.19272	1.013	0.09639	\CCOC10
58	690.74	663.801	4.696	0.80558	4.0016	0.38075	\CCC12
57	675.59	649.242	1.4156	0.24284	6.6709	0.63472	\OCCC11
56	658.61	632.924	11.9842	2.05583	14.7621	1.40459	\CCC12
55	636.45	611.628	13.4297	2.3038	2.7499	0.26165	\CCC12
54	617.96	593.86	4.2629	0.73128	9.9248	0.94433	\CCC12
53	615.66	591.649	1.528	0.26212	7.6639	0.72921	\CCC12
52	605.48	581.866	25.5533	4.38354	11.8043	1.12316	\CCC16
51	598.4	575.062	8.7127	1.49462	0.3905	0.03716	\CCC11
50	585.83	562.983	25.0641	4.29962	11.8209	1.12474	\CCC11
49	571.56	549.269	4.1685	0.71509	2.6385	0.25105	\CCC11
48	561.98	540.063	7.4439	1.27696	4.6129	0.43891	\CCC11
47	529.74	509.08	0.3807	0.06531	4.7889	0.45566	\OCC16
46	517	496.837	12.7913	2.19428	11.1347	1.05945	\OCC16
45	483.6	464.74	8.1116	1.39151	7.1576	0.68103	\COC10
44	469.62	451.305	17.518	3.00513	2.535	0.2412	\OCC11
43	465.69	447.528	2.2645	0.38846	1.8741	0.17832	\CCC11 + \OCC12
42	455.4	437.639	2.4131	0.41396	1.9208	0.18276	\HOCC10
41	446.74	429.317	192.078	32.95	2.8012	0.26653	\HOCC10
40	433.29	416.392	17.119	2.93668	3.2685	0.31099	\HOCC10
39	431	414.191	58.4175	10.0212	4.5151	0.4296	\HOCC13
38	423.92	407.387	50.8994	8.73154	3.2905	0.31309	\HOCC29
37	416.67	400.42	34.3882	5.89913	5.7354	0.54571	\HOCC90
36	411.25	395.211	81.8484	14.0407	0.9393	0.08937	\HOCC90
35	403.26	387.533	116.007	19.9004	1.0516	0.10006	\HOCC90
34	386.74	371.657	16.3816	2.81018	11.1087	1.05697	\HOCC90
33	378.97	364.19	6.213	1.06581	1.884	0.17926	\OCCC10
32	372.73	358.194	3.8804	0.66566	2.2366	0.21281	\CCC17 + \OCC18
31	348.11	334.534	65.0279	11.1552	1.9364	0.18425	\HOCC60
30	346.26	332.756	40.3214	6.91694	1.7639	0.16783	\HOCC60
29	336.72	323.588	7.517	1.2895	2.3298	0.22168	\HOCC60
28	327.44	314.67	3.6346	0.6235	0.9718	0.09247	\HOCC60
27	311.51	299.361	4.2485	0.72881	0.5066	0.0482	\OCC26
26	305.06	293.163	6.3213	1.08439	0.0376	0.00358	\OCC26
25	290.56	279.228	8.0025	1.37279	1.9549	0.18601	\CCCC27
24	265.84	255.472	14.3476	2.46126	1.5795	0.15029	\OCC36
23	263.32	253.051	8.7875	1.50745	1.0866	0.10339	\OCC36
22	258.79	248.697	2.5513	0.43766	0.5627	0.05354	\CCCO13

21	248.13	238.453	24.94	4.27833	1.41	0.13416	νCCC11 + νHOCC13
20	244.33	234.801	48.0298	8.23928	0.6171	0.05872	νCC11
19	232.49	223.423	62.6991	10.7557	1.5399	0.14652	νCC11
18	227.91	219.022	10.127	1.73724	1.3463	0.1281	νCC11
17	222.7	214.015	8.4618	1.45158	2.8059	0.26698	νCCCC32
16	199.72	191.931	5.5246	0.94772	5.3172	0.50592	νCCCC32
15	187.01	179.717	2.1046	0.36103	0.6276	0.05972	νCCO28
14	174.58	167.771	1.3182	0.22613	1.0614	0.10099	νOCO11
13	140.29	134.819	2.5487	0.43722	0.8921	0.08488	νCCOC14
12	132.2	127.044	0.5884	0.10094	0.7244	0.06893	νOCC10
11	119.58	114.916	0.9859	0.16913	0.2501	0.0238	νOCCC13
10	117.44	112.86	0.8457	0.14508	0.1582	0.01505	νCOCC11
9	102.98	98.9638	2.3414	0.40166	0.41	0.03901	νOCC 12
8	87.48	84.0683	1.4036	0.24078	1.2029	0.11445	νOCC 12
7	67.5	64.8675	0.4643	0.07965	1.9087	0.18161	νOCC 12
6	59.37	57.0546	1.9509	0.33467	1.8421	0.17527	νOCC 12
5	42.78	41.1116	0.8005	0.13732	1.7286	0.16447	νCOCC 14
4	38.78	37.2676	0.9588	0.16448	3.4832	0.33142	νCOCC 14
3	28.3	27.1963	0.6116	0.10492	3.0906	0.29407	νCOCC 14
2	20.57	19.7678	0.3043	0.0522	2.2566	0.21471	νCOCC 14
1	12.17	11.6954	0.1841	0.03158	0.819	0.07793	νOCOC 73

and O9 – H50 – O8 (148.0°) further confirm strong hydrogen-bond interactions. The smallest angle, C13 – O3 – H42 (81.9°), reflects angular strain around the hydroxyl group. Aromatic ring angles such as C24 – C28 – C32 (120.1°), C28 – C32 – C33 (120.4°) and C26 – C30 – C29 (121.9°) remain close to the ideal 120°, confirming planarity and ring stability. Overall, the optimized geometric parameters indicate that 5H3M1P1C4O possesses a stable and well-defined molecular structure, supported by favourable bond lengths, bond angles, and intramolecular hydrogen bonding, which are crucial for its electronic behaviour and potential biological interactions[14-17].

Vibrational assignment

A PerkinElmer FT-IR spectrophotometer

Table 3: Reactivity profile and molecular stability

Quantum Chemical Parameter	Gas Phase	Water	Methanol (MeOH)	Ethanol (EtOH)	DMSO
HOMO Energy (eV)	-6.729	-6.254	-6.256	-6.258	-6.255
LUMO Energy (eV)	-2.368	-2.281	-2.281	-2.281	-2.281
Ionization Energy (eV)	6.729	6.254	6.256	6.258	6.255
Electron Affinity Value (eV)	2.368	2.281	2.281	2.281	2.281
HOMO–LUMO Separation (eV)	4.361	3.973	3.975	3.977	3.974
Absolute Electronegativity (χ)	4.549	4.268	4.269	4.270	4.268
Electronic Chemical Potential (μ)	-4.549	-4.268	-4.269	-4.270	-4.268
Chemical Hardness (η)	2.181	1.987	1.988	1.989	1.987
Chemical Softness (S)	0.229	0.252	0.252	0.251	0.252
Electrophilic Reactivity Index (ω)	4.744	4.584	4.584	4.584	4.584
Electronic Charge Transfer (ΔN)	2.086	2.148	2.148	2.147	2.148
Electron Donation Power (ω^-)	7.291	6.966	6.966	6.967	6.966
Electron Acceptance Power (ω^+)	2.742	2.698	2.698	2.697	2.698

was used to record the 5H3M1P1C4O FT-IR spectrum in the 4000-500 cm^{-1} range, while a Bruker RFS Raman spectrometer was used to analyze the FT-Raman spectrum in the 3500-500 cm^{-1}.[18] Density functional theory was used at the B3LYP/6-311++G(d,p) level to determine the theoretical vibrational frequencies. An improvement in concordance between the experimental and theoretical spectra was seen after scaling all calculated frequencies by a factor of 0.961 to account for anharmonicity and basis-set shortcomings[19]. Nonlinear (3N-6) normal vibrational modes are generated by the N atoms in the studied molecule. In order to determine the modes, the VEDA4 algorithm conducted a potential energy distribution (PED) study. [20] Table 2 summarizes the tested FT- IR and FT-Raman frequencies, their corresponding scaled theoretical values, and the PED contributions. As seen in Figure 2, the experimental and simulated spectra are correlated[21]. The influences of solid states, interactions between molecules, temperature fluctuations, and instrumental resolution can cause small differences in observed and theoretical frequency. The experimental spectra show some weak irregularities, which are explained by instrumental noise[22-24].

O–H and C–H vibrations

Phenolic O–H stretching vibrations are characteristically broad due to strong intra- and intermolecular hydrogen bonding, typically appearing in the region 3600–3200 cm^{-1}. In the present compound, a broad absorption envelope observed between 3350 and 3200 cm^{-1} in the FT-IR spectrum is assigned to O–H stretching modes of hydroxyl groups attached to the chromen-4-one and glycosidic moieties. This broad nature is well reproduced in the simulated spectrum after appropriate scaling and band broadening, confirming extensive hydrogen-bonding interactions in the molecular framework[25].

In general, the region of 3100-2850 cm^{-1} is where you may see aromatic and aliphatic C-H stretching vibrations. The aromatic rings' and sugar units' C-H stretching modes are mapped to the area of 5H3M1P1C4O's FT-IR spectrum where bands of weak to medium intensity are observed. The greater Raman activity of these modes causes them to show up more strongly in the FT-Raman spectrum, especially for symmetric stretching vibrations. The experimental assignments are supported by theoretical calculations that indicate these modes exist between 3080 and 2890 cm^{-1}, with PED contributions surpassing 85%[25].

C=O and C–O stretching vibrations

The carbonyl (C=O) stretching vibration is a key spectral marker of chromen-4-one derivatives and typically appears between 1700 and 1650 cm^{-1}. In the FT-IR spectrum of the present compound, a strong absorption band observed in the region 1660–1630 cm^{-1} is attributed to the C = O stretching vibration of the chromen-4-one ring. The corresponding Raman band appears with moderate intensity, consistent with partial symmetry reduction due to substitution effects. Theoretical calculations locate this vibration in the 1685–1650 cm^{-1} range, with PED contributions of approximately 60–70%, supporting the experimental observation. C–O stretching vibrations associated with phenolic, ether and glycosidic linkages are expected in the 1300–1000 cm ^{1} region. Experimentally, prominent FT-IR bands observed near 1260, 1210 and 1080 cm ^{1}, along with corresponding Raman bands, are assigned to these modes. Theoretical frequencies predicted between 1280 and 1050 cm^{-1}, with PED contributions ranging from 40% to 65%, further confirm these assignments[26].

C–C skeletal vibrations

Within the 1600-1000 cm^{-1} range, you may often find aromatic C-C stretching vibrations. According to the FT-IR spectra, the conjugated aromatic system's C-C stretching modes are represented by bands at around 1580, 1490, 1380 and 1270 cm^{-1}. These vibrations stand out more in the FT-Raman spectrum because they are symmetric and have a delocalized π-electron character. Coherent C-C skeletal vibrations in the 1575-1265 cm^{-1} range are predicted by theoretical calculations, with PED contributions ranging from 30% to 55%, suggesting moderate mode mixing with neighboring bending movements[11,12,24,26].

Bending and deformation vibrations

C–H in-plane and out-of-plane bending vibrations are typically observed between 1450 and 1000 cm^{-1}. In the present compound, these modes are clearly detected in both FT-IR and FT-Raman spectra and are theoretically predicted in the region

Table 4: Assessment of Fock Matrix stabilization energies using second-order Perturbation method in 5H3M1P1C4O

Donor Orbital Energy (Ed/e)	Orbital type	Donor orbital	Donor Orbital Energy (Ed/e)	Orbital type	Acceptor orbital	Second-order stabilization energy E(2) kcal/mol a.u	Energy Gap ΔE = E(j) - E(i)b a.u	Fock Matrix Element (i,j) in a.u.
1.99406	σ	O12-C33	0.04393	σ*	C17-H38	856.93	0.23	0.398
1.96896	σ	C24-C28	0.04393	σ*	C17-H38	830.46	0.05	0.178
1.9724	σ	C27-C31	0.04393	σ*	C17-H38	769.07	0.06	0.197
1.98856	σ	O12-H53	0.39662	π*	C32-C33	442.73	0.79	0.587
1.99406	σ	O12-C33	0.39662	π*	C32-C33	438.64	1.42	0.787
1.98856	σ	O12-H53	0.03272	σ*	C16-H37	417.23	0.07	0.158
1.99325	σ	O11-C31	0.04393	σ*	C17-H38	354.98	0.27	0.278
1.96457	σ	C24-C27	0.04393	σ*	C17-H38	317.11	0.04	0.103
1.98688	σ	O11-H52	0.0124	σ*	C27-H46	284.55	3.67	0.912
1.99406	σ	O12-C33	0.03272	σ*	C16-H37	263.5	0.71	0.389
1.97661	LP1	O12	0.03272	σ*	C16-H37	259.5	0.5	0.321
1.99325	νσ	O11-C31	0.0124	σ*	C27-H46	236.09	3.88	0.855
1.97754	νσ	C32-C33	0.03272	σ*	C16-H37	214.83	0.57	0.314
1.97661	LP1	O12	0.39662	π*	C32-C33	200.51	1.21	0.488
0.36493	π*	O8-C21	0.26917	π*	C19-C20	190.94	0.01	0.077
0.41857	π*	C26-C30	0.47033	π*	C22-C23	160.67	0.02	0.081
1.97764	σ	C32-H49	0.03272	σ*	C16-H37	151.99	0.37	0.211
1.97149	νσ	C31-C33	0.03272	σ*	C16-H37	142.85	0.56	0.253
1.97785	LP1	O11	0.0124	σ*	C27-H46	134.87	3.57	0.621
1.97754	σ ν	C32-C33	0.02011	σ*	C27-C31	127.04	0.31	0.176
1.99406	σ	O12-C33	0.02986	σ*	C16-C18	112.27	0.94	0.291
1.97661	LP1	O12	0.02986	σ*	C16-C18	102.32	0.72	0.243
1.97754	σ ν	C32-C33	0.02986	σ*	C16-C18	96.62	0.8	0.248
1.97661	LP1	O12	0.39662	π*	C32-C33	200.51	1.21	0.488
0.36493	π*	O8-C21	0.26917	π*	C19-C20	190.94	0.01	0.077
0.41857	π*	C26-C30	0.47033	π*	C22-C23	160.67	0.02	0.081
1.97764	σ	C32-H49	0.03272	σ*	C16-H37	151.99	0.37	0.211
1.97149	σ	C31-C33	0.03272	σ*	C16-H37	142.85	0.56	0.253
1.97785	LP1	O11	0.0124	σ*	C27-H46	134.87	3.57	0.621
1.97754	σ	C32-C33	0.02011	σ*	C27-C31	127.04	0.31	0.176
1.99406	σ	O12-C33	0.04393	σ*	C17-H38	856.93	0.23	0.398
1.96896	σ	C24-C28	0.04393	σ*	C17-H38	830.46	0.05	0.178
1.9724	σ	C27-C31	0.04393	σ*	C17-H38	769.07	0.06	0.197
1.98856	σ	O12-H53	0.39662	π*	C32-C33	442.73	0.79	0.587
1.99406	σ	O12-C33	0.39662	π*	C32-C33	438.64	1.42	0.787
1.98856	σ	O12-H53	0.03272	σ*	C16-H37	417.23	0.07	0.158
1.99325	σ	O11-C31	0.04393	σ*	C17-H38	354.98	0.27	0.278
1.96457	σ	C24-C27	0.04393	σ*	C17-H38	317.11	0.04	0.103
1.98688	σ	O11-H52	0.0124	σ*	C27-H46	284.55	3.67	0.912
1.99406	σ	O12-C33	0.03272	σ*	C16-H37	263.5	0.71	0.389
1.97661	LP1	O12	0.03272	σ*	C16-H37	259.5	0.5	0.321

1.99325	σ	O11-C31	0.0124	σ*	C27-H46	236.09	3.88	0.855
1.97754	σ	C32-C33	0.03272	σ*	C16-H37	214.83	0.57	0.314
1.97661	LP1	O12	0.39662	π*	C32-C33	200.51	1.21	0.488
0.36493	π*	O8-C21	0.26917	π*	C19-C20	190.94	0.01	0.077
0.41857	π*	C26-C30	0.47033	π*	C22-C23	160.67	0.02	0.081
1.97764	σν	C32-H49	0.03272	σ*	C16-H37	151.99	0.37	0.211
1.97149	νσ	C31-C33	0.03272	σ*	C16-H37	142.85	0.56	0.253
1.97785	LP1	O11	0.0124	σ*	C27-H46	134.87	3.57	0.621
1.97754	σ ν	C32-C33	0.02011	σ*	C27-C31	127.04	0.31	0.176

Table 5: NBO hybrid orbital composition and electron density distribution of selected Lewis orbitals in the 5H3M1P1C4O

$\frac{\text{Bond(A-B)/Ip}}{(ED_{A-B})/(ED_{IP})}$	EDA%/ EDB%	NBO hybrid / orbitals	s,p %
ν(O1-C16)	68.29	.8264(sp2.58)O	27.89, 72.06
1.98039	31.71	.5631(sp4.18)C	19.25, 80.45
ν(O1-C17)	67.31	.8204(sp2.51)O	28.46, 71.48
1.98661	32.69	0.5717(sp3.44)C	22.46, 77.27
ν(C32-H49)	60.52	0.778(sp2.48)C	28.72, 71.24
1.97764	39.48	.6283(sp0)H	99.95, 0.05

1480–1010 cm^{-1}, with PED contributions ranging from 70% to 90%, indicating well-defined bending character[11-12].

Skeletal deformation modes involving C–C–C and O–C–C bending vibrations are mainly located below 1000 cm^{-1}. Experimentally, bands observed around 900, 780, 650 and 550 cm^{-1} are attributed to these deformation modes. Theoretical calculations place these vibrations between 950 and 300 cm^{-1}, with PED contributions of 40–80%, supporting the experimental assignments and confirming the structural rigidity of the molecular backbone.

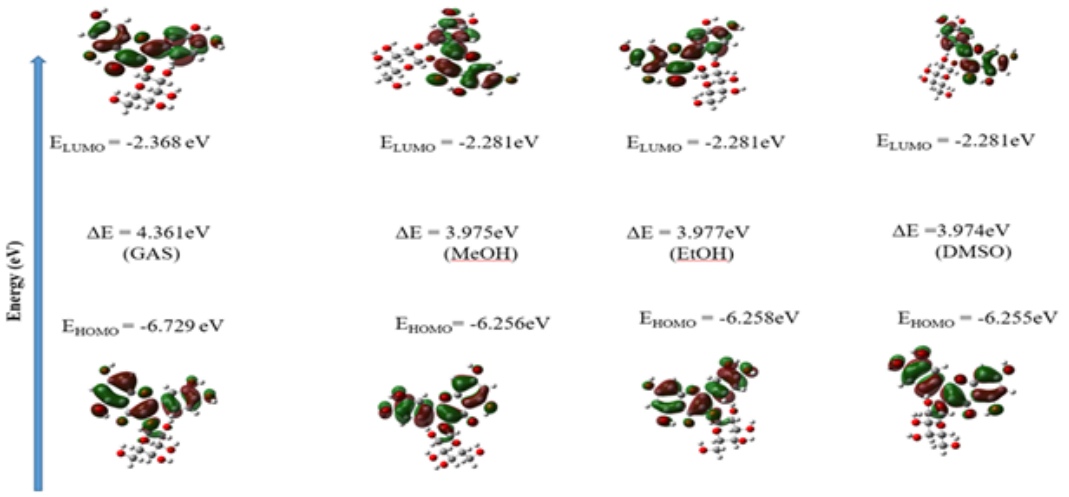


Fig. 3: Effect of solvent environment on HOMO–LUMO energy levels of 5H3M1P1C4O

Spectral correlation

Overall, the scaled DFT-calculated FT-IR and FT-Raman spectra show good agreement with the experimental results. Minor deviations between calculated and observed frequencies can be attributed to anharmonic effects, intermolecular hydrogen bonding, and solid-state interactions not fully accounted for in the gas-phase calculations. The successful correlation between experimental and theoretical vibrational data confirms the structural integrity of 5H3M1P1C4O and validates the reliability of the adopted computational methodology.

Frontier molecular orbital (FMO) analysis: (Study of HOMO–LUMO)

Frontier molecular orbitals (FMOs), namely the highest occupied molecular orbital (HOMO) and the lowest unoccupied molecular orbital (LUMO), play a crucial role in understanding the electronic structure, stability and reactivity of molecular systems. Analysis of the HOMO and LUMO energies provide valuable insight into the kinetic stability, chemical reactivity, optical polarizability, softness and hardness of a compound. These parameters are also closely associated with charge transfer processes and potential biological interactions.

Table 6: Experimental and time-dependent DFT Study of the electronic excited states of 5H3M1P1C4O

Exp. Wave length (nm)	Band Gap (eV)	Solv-ents	Energy (cm^{-1})	Theo. Wave length (nm)	Energy Gap (ΔE) (eV)	Oscillator Strength	Electronic State Symmetry	Major contribution
330	3.76	gas	27983.40591	357.3546419	3.47	0.1664	Singlet-A	HOMO-> LUMO (92%)
			31466.10794	317.8022531	3.9	0.2375	Singlet-A	H-1->LUMO (92%)
			32422.68149	308.4260629	4.02	0.0006	Singlet-A	H-6->LUMO (80%)
350	3.54	Me- OH	27900.33081	358.4186893	3.46	0.3775	Singlet-A	HO MO-> LUMO (93%)
			30500.66229	327.8617332	3.78	0.116	Singlet-A	H-1->LUMO (93%)
			33283.27507	300.451202	4.13	0.0618	Singlet-A	H-5->LUMO (21%), H-3->LUMO (15%), H-2->LUMO (56%)
360	3.44	Et- OH	27900.33081	358.4186893	3.46	0.3775	Singlet-A	HO MO-> LUMO (93%)
			30500.66229	327.8617332	3.78	0.116	Singlet-A	H-1->LUMO (93%)
			33283.27507	300.451202	4.13	0.0618	Singlet-A	H-5->LUMO (21%), H-3->LUMO (15%), H-2->LUMO (56%)

Table 7: Computational study of local softness and dual reactivity indices in 5H3M1P1C4O

	Mulliken atomic charges			Fukui functions			Fukui functions			
Atom	**0, 1 (N)**	**N+1 (-1, 2)**	**N-1 (1,2)**	**fr+**	**fr-**	**fr0**	**Δfr**	**sr+ $fr+$**	**sr-$fr-$**	**sr^0 fr^0**
1O	-0.01068	-0.00116	-	0.010	-0.005	0.002	0.014	0.002	-0.001	0.001
2O	0.018039	-0.00501	0.057984	-0.023	-0.040	-0.031	0.017	-0.005	-0.009	-0.007
3O	-	-0.227663	-	-0.017	-0.023	-0.020	0.007	-0.004	-0.005	-0.004
4O	-	-0.167446	-	-0.006	-0.008	-0.007	0.002	-0.001	-0.002	-0.002
5O	-	-0.243562	-	-0.020	-0.026	-0.023	0.006	-0.004	-0.006	-0.005
6O	-	-0.248266	-	-0.015	-0.022	-0.018	0.007	-0.003	-0.005	-0.004
7O	0.049596	0.006853	0.091724	-0.043	-0.042	-0.042	-0.001	-0.009	-0.009	-0.009
8O	-	-0.422319	-	-0.113	-0.053	-0.083	-0.060	-0.025	-0.012	-0.018
9O	-	-0.282931	-	-0.045	-0.075	-0.060	0.030	-0.010	-0.016	-0.013
10O	-	-0.240479	-	-0.037	-0.045	-0.041	0.008	-0.008	-0.010	-0.009
11O	-	-0.250443	-	-0.026	-0.046	-0.036	0.020	-0.006	-0.010	-0.008
12O	-	-0.328074	-	-0.037	-0.052	-0.045	0.015	-0.008	-0.011	-0.010
13C	-0.29772	-0.308481	-	-0.011	-0.002	-0.007	-0.008	-0.002	-0.001	-0.001
14C	-	-0.356585	-	0.002	-0.003	-0.001	0.006	0.000	-0.001	0.000
15C	-	-0.574056	-	0.026	0.011	0.019	0.015	0.006	0.002	0.004
16C	-0.01619	0.025243	-	0.041	0.042	0.042	-0.001	0.009	0.009	0.009
17C	-	-0.29122	-	0.029	0.056	0.043	-0.028	0.006	0.012	0.009
18C	-	-0.438446	-	-0.032	-0.028	-0.030	-0.004	-0.007	-0.006	-0.007
19C	0.394348	0.340841	0.473679	-0.054	-0.079	-0.066	0.026	-0.012	-0.017	-0.014
20C	-0.53715	-0.577915	-	-0.041	-0.014	-0.028	-0.026	-0.009	-0.003	-0.006
21C	0.289052	0.197712	0.309788	-0.091	-0.021	-0.056	-0.071	-0.020	-0.005	-0.012
22C	0.708338	0.668081	0.768894	-0.040	-0.061	-0.050	0.020	-0.009	-0.013	-0.011
23C	-	-0.402689	-	0.010	0.011	0.010	-0.001	0.002	0.002	0.002
24C	0.388096	0.395721	0.414527	0.008	-0.026	-0.009	0.034	0.002	-0.006	-0.002
25C	-	-0.036581	0.013459	-0.031	-0.019	-0.025	-0.013	-0.007	-0.004	-0.005
26C	-0.43701	-0.455734	-	-0.019	-0.049	-0.034	0.030	-0.004	-0.011	-0.007
27C	0.112514	0.087299	0.121774	-0.025	-0.009	-0.017	-0.016	-0.005	-0.002	-0.004
28C	-	-0.348737	-	-0.068	-0.032	-0.050	-0.035	-0.015	-0.007	-0.011
29C	-	-0.008255	-	0.014	-0.011	0.001	0.026	0.003	-0.002	0.000
30C	-	-0.534106	-	0.017	0.030	0.023	-0.013	0.004	0.007	0.005
31C	-	-0.379118	-	0.025	0.022	0.024	0.003	0.006	0.005	0.005
32C	0.132265	0.086159	0.164996	-0.046	-0.033	-0.039	-0.013	-0.010	-0.007	-0.009
33C	-	-0.284319	-	-0.048	-0.028	-0.038	-0.020	-0.010	-0.006	-0.008
34H	0.220642	0.21275	0.23189	-0.008	-0.011	-0.010	0.003	-0.002	-0.002	-0.002
35H	0.233727	0.208046	0.26025	-0.026	-0.027	-0.026	0.001	-0.006	-0.006	-0.006
36H	0.310178	0.297186	0.323083	-0.013	-0.013	-0.013	0.000	-0.003	-0.003	-0.003
37H	0.191947	0.183313	0.203497	-0.009	-0.012	-0.010	0.003	-0.002	-0.003	-0.002
38H	0.266009	0.282077	0.272174	0.016	-0.006	0.005	0.022	0.004	-0.001	0.001
39H	0.19258	0.181861	0.204588	-0.011	-0.012	-0.011	0.001	-0.002	-0.003	-0.002
40H	0.191618	0.172675	0.211114	-0.019	-0.019	-0.019	0.001	-0.004	-0.004	-0.004
41H	0.267403	0.267071	0.268521	0.000	-0.001	-0.001	0.001	0.000	0.000	0.000
42H	0.260044	0.254509	0.265874	-0.006	-0.006	-0.006	0.000	-0.001	-0.001	-0.001
43H	0.335272	0.349765	0.324732	0.014	0.011	0.013	0.004	0.003	0.002	0.003
44H	0.264015	0.27421	0.254978	0.010	0.009	0.010	0.001	0.002	0.002	0.002
45H	0.144256	0.110374	0.189544	-0.034	-0.045	-0.040	0.011	-0.007	-0.010	-0.009

46H	0.245639	0.217867	0.262173	-0.028	-0.017	-0.022	-0.011	-0.006	-0.004	-0.005
47H	0.219224	0.191087	0.244437	-0.028	-0.025	-0.027	-0.003	-0.006	-0.005	-0.006
48H	0.218477	0.173681	0.262683	-0.045	-0.044	-0.045	-0.001	-0.010	-0.010	-0.010
49H	0.165247	0.118982	0.205164	-0.046	-0.040	-0.043	-0.006	-0.010	-0.009	-0.009
50H	0.331162	0.323895	0.341306	-0.007	-0.010	-0.009	0.003	-0.002	-0.002	-0.002
51H	0.272274	0.256592	0.286162	-0.016	-0.014	-0.015	-0.002	-0.003	-0.003	-0.003
52H	0.284629	0.266622	0.299652	-0.018	-0.015	-0.017	-0.003	-0.004	-0.003	-0.004
53H	0.284986	0.263116	0.305226	-0.022	-0.020	-0.021	-0.002	-0.005	-0.004	-0.005

For the title compound 5H3M1P1C4O, the calculated HOMO and LUMO energies in the gas phase are –6.729 eV and –2.368 eV, respectively, resulting in an energy gap (ΔE) of 4.361 eV. This moderate HOMO–LUMO gap indicates good molecular stability along with appreciable chemical reactivity. Upon solvation in polar media such as methanol, ethanol, and DMSO, the HOMO energy shifts to –6.256 eV, –6.258 eV and –6.255 eV respectively, while the LUMO energy stabilizes at –2.281 eV in all solvent environments. Consequently,

Table 8: Computational Investigation of NLO Characteristics of 5H3M1P1C4O

Parameter	B3LYP/6-311++G(d,p)	Parameter	B3LYP/6-311++G(d,p)
μx	1.1598463	β	-728.7821815
μy	3.3593608	βxxy	431.5888174
μz	0.2408685	βxyy	374.1637194
μ(D)	3.562101354	βyyy	-2247.860405
αxx	213.028	βzxx	-90.2845594
αxy	-7.9288341	βxyz	39.8321483
αyy	399.9339353	βzyy	187.0148623
αxz	27.3846318	βxzz	-22.5386529
αyz	-6.5363008	βyzz	-43.7891065
αzz	190.5032663	βzzz	24.1094624
α(a.u)	267.8217339	βtot (a.u)	1901.755905
α(e.s.u)	3.9691E-23	βtot (e.s.u)	1.6430E-29
Δα(a.u)	419.2779329	mz	0.2408685
Δα (e.s.u)	6.2137E-23	m(D)	3.562101354

Table 9: Evaluation of the Physicochemical Properties of 5H3M1P1C4O

Physicochemical Properties		Drug-Likeness	
Lipophilicity Index (WLOGP)	-0.54	Bio availability score	0.17
Molecular weight	464.38 g/mol	Pharmacokinetics	
Log S	-3.04	GI absorption	LOW
Number of aromatic heavy	16	BBB permeant	NO
Fraction Csp3	0.29	P-gp substrate	NO
Number of rotatable bonds	4	Log Kp (skin permeation)	-8.88 cm/ s
Number of H-bond acceptors	12		
Number of H-bond donors	8		
Molar refractivity	110.16		
TPSA	210.51 A2		

TPSA: Topological Polar Surface Area; BBB: Blood-brain barrier penetration; log kp: skin permeability

Table 10: Molecular docking analysis of 5H3M1P1C4O with target proteins

Protein (PDB ID)	Source Organism	Binding Energy (kcal/mol)	Inhibition Constant (μM)	Inter molecular energy (kcal/mol)	Electrostatic energy (kcal/mol)	Total internal energy (kcal/mol)	Reference RMSD (Å)
3ERT	Homosapien	-4.29	712.31	-7.87	-0.28	-8.48	37.26
6J90	Homosapien	-4.25	766.68	-7.83	-0.62	-6.96	58.83
7RPU	Homosapien	-5.23	147.73	-8.81	-0.48	-6.18	94.78
8TSK	Homosapien	-3.67	2.03	-7.25	-0.14	-6.48	40.69

Table 11: Molecular docking–derived binding energies and major non-covalent interactions of ligand 5H3M1P1C4O with selected antineoplastic target proteins

Protein	B.E energy (kcal/mol)	Interacting residues	Type of interaction	Distance (Å)
3ERT	–4.29	VAL12, LEU13	Hydrophobic	3.5–4.5
		ILE10, TYR5	π–Alkyl / π–π	3.8–4.2
		LYS11, LYS21	Hydrogen bond	2.0–2.8
		SER9	Hydrogen bond	2.1–2.6
6J90	–4.25	GLU31	Hydrogen bond	2.0–2.7
		TYR52, TRP38	π–π stacking	3.6–4.1
		LEU35, ALA32	Hydrophobic	3.7–4.6
7RPU	–5.23	HIS41	Hydrogen bond	2.0–2.5
		LEU27, VAL25	Hydrophobic	3.6–4.4
		PHE48	π–√ π–Alkyl	3.8–4.2
8TSK	–3.67	SER88	Hydrogen bond	2.1–2.7
		TYR90, PHE92	π–σ/ π–Alkyl	3.7–4.3
		LEU85	Hydrophobic	3.8–4.6

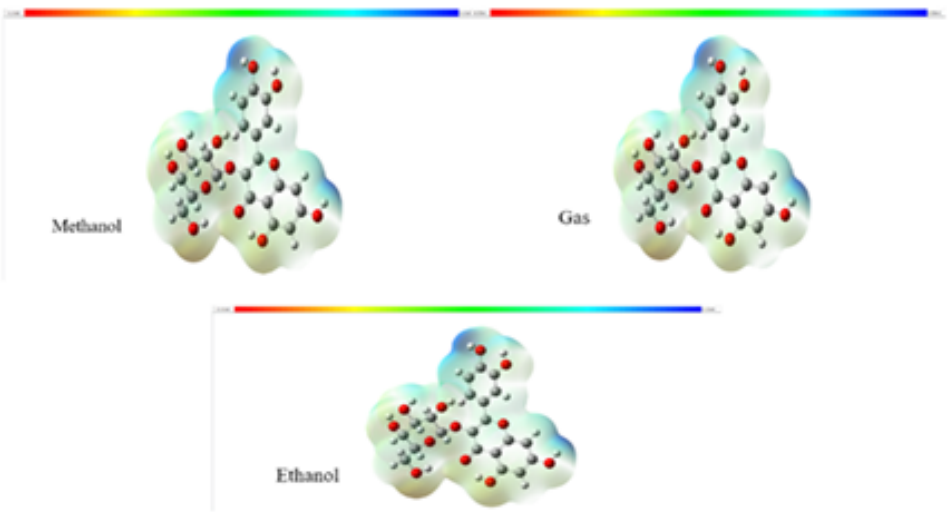


Fig. 4: Molecular electrostatic potential of 5H3M1P1C4O for different solvents

the HOMO–LUMO energy gap decreases to 3.975 eV (MeOH), 3.977 eV (EtOH) and 3.974 eV (DMSO), indicating enhanced electronic delocalization and increased reactivity in solution. The calculated frontier orbital energies and global reactivity descriptors in the gas phase and solvent media are summarized in Table 3.

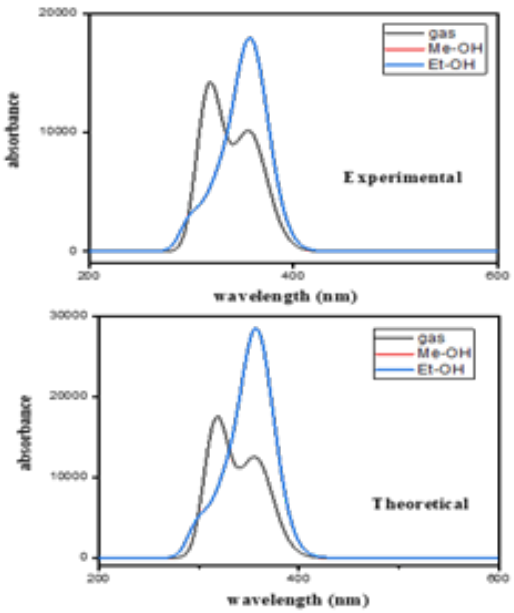


Fig. 5: Theoretical and experimental UV–Visible spectral analysis of 5H3M1P1C4O

The reduced HOMO–LUMO gap observed in solvent environments facilitates easier excitation of electrons from the HOMO to the LUMO, which is a desirable feature for intramolecular charge transfer and nonlinear optical (NLO) activity. Moreover, the relatively low energy gap values (< 5eV) obtained for 5H3M1P1C4O in all media suggest potential biological activity, as compounds with smaller band gaps generally exhibit improved redox behavior and enhanced ability to participate in biochemical interactions such as electron donation, electron acceptance and binding to enzyme or receptor active sites.

The solvent effect on the electronic properties of 5H3M1P1C4O was examined using the IEFPCM solvation model, considering polar solvents due to their ability to stabilize the electronic cloud of the molecule. Although slight stabilization of the frontier orbital energies is observed in solvent media, the overall changes remain marginal, indicating that the intrinsic electronic structure of the molecule is largely preserved. The spatial distributions of the HOMO and LUMO orbitals for the gas phase, methanol, ethanol and DMSO are illustrated in Fig. 3. The HOMO density is predominantly localized over electron-rich regions of the molecular framework, whereas the LUMO density is mainly distributed over electron-deficient regions, confirming effective

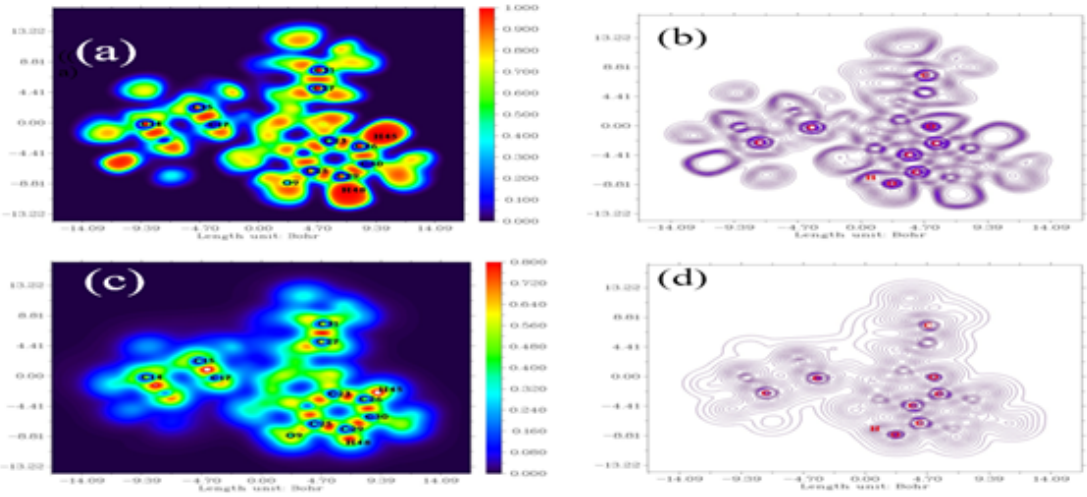


Fig. 6: (a, b) Electron localization function (ELF) contour and colour-filled maps with gradient lines, and (c, d) localized orbital locator (LOL) contour and colour-filled maps with gradient lines for 5H3M1P1C4O in the gas phase

intramolecular charge transfer. The similarity in orbital shapes across different environments highlights the solvent-independent nature of the electronic distribution.

The ionization potential decreases from 6.729 eV in the gas phase to approximately 6.25 eV in solvent media, indicating that electron removal becomes energetically more favourable in solution. Similarly, the electron affinity slightly decreases upon solvation, reflecting moderate stabilization of the LUMO level. These observations collectively confirm the enhanced charge transfer capability of 5H3M1P1C4O in polar solvents.

The electrophilicity index remains relatively high and nearly constant across all solvent environments, confirming the pronounced electrophilic character of the molecule and its strong tendency to interact with electron-rich biomolecular sites. Additionally, the decrease in chemical hardness accompanied by an increase in chemical softness in solvent media indicates improved molecular reactivity and polarizability. The low chemical potential values further suggest that the system remains thermodynamically stable and close to equilibrium. Overall, the frontier molecular orbital analysis and global reactivity descriptors presented in Table 3, together with the HOMO–LUMO visualizations shown in Fig. 3, demonstrate that 5H3M1P1C4O possesses favourable electronic characteristics, solvent-enhanced reactivity, strong electrophilic behaviour and promising optical as well as biological interaction potential.

Charge distribution (MEP) analysis

The molecular electrostatic potential (MEP) surface provides valuable insight into the charge distribution and solvation behaviour of the molecule. Although pronounced negative electrostatic potential regions are observed around the oxygen atoms of the hydroxyl and carbonyl groups, these electron-rich sites are spatially localized and do not extend over the entire molecular framework. The remaining aromatic and heterocyclic regions exhibit comparatively neutral to positive potential, indicating a dominant nonpolar character.

Despite the presence of multiple oxygen atoms capable of hydrogen bonding, the overall MEP pattern suggests limited interaction with highly polar solvents such as water. The absence of extensive, continuous negative potential regions restricts strong hydration and reduces favourable solute–solvent interactions. Consequently, the molecule exhibits poor affinity towards water molecule, explaining its observed insolubility in aqueous media.

In contrast, moderate stabilization of charge-separated regions in less polar solvents were reflected by slightly enhanced electrostatic potential values, while the overall charge distribution remains unchanged. This behavior indicates that the intrinsic electronic structure governs solubility characteristics. Therefore, the combined presence of localized polar sites and an extended hydrophobic framework account for the water insolubility of 5H3M1P1C4O.

The molecular electrostatic potential values of 5H3M1P1C4O were obtained directly from the color scale shown at the top of the MEP surface plots. In the gas phase, the electrostatic potential ranges from -8.535×10^{2} to $+8.535 \times 10^{2}$ a.u. In both ethanol and methanol solvent environments, a wider potential distribution is observed, extending from -0.101×10^{0} to $+0.101 \times 10^{0}$ a.u. This increase in the potential range in polar protic solvents indicates enhanced polarization of the molecule due to solvent–solute interactions, as reflected in the MEP surfaces.

Natural bond orbital (NBO) analysis

Natural Bond Orbital analysis was carried out to investigate intramolecular charge transfer and the stabilization effects arising from donor–acceptor interactions in the molecule. The second-order perturbation treatment of the Fock matrix quantitatively describes the delocalization of electron density from filled (Lewis) orbitals to unoccupied antibonding (non-Lewis) orbitals, thereby revealing the origin of molecular stabilization.

As presented in Table 4, several significant donor–acceptor interactions contribute to the overall stability of the system. The strongest stabilization is observed for the σ(O12–C33) $\rightarrow$ σ^*(C17–H38) interaction, with a stabilization energy of 856.93 kcal/mol. Comparable $\sigma \rightarrow \sigma^*$ interactions include σ(C24–C28) $\rightarrow$ σ^*(C17–H38) and σ(C27–C31) $\rightarrow$ σ^*(C17–H38), exhibiting stabilization energies of 830.46 and 769.07 kcal/mol, respectively. These high E(2) values indicate substantial hyper conjugative

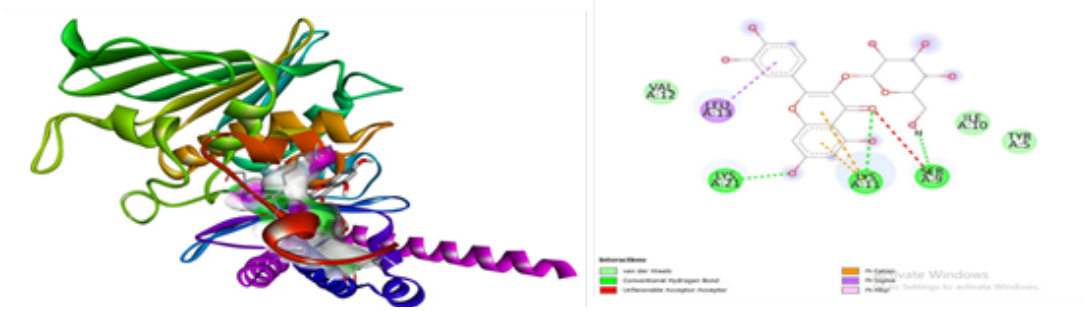


Fig. 8: 3D and 2D Molecular docking of compound 5H3M1P1C4O with 3ERT protein

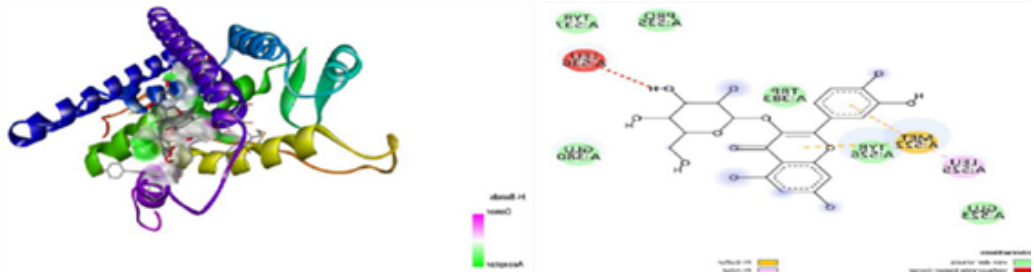


Fig. 9: 3D and 2D Molecular docking of compound 5H3M1P1C4O with 6J90 protein

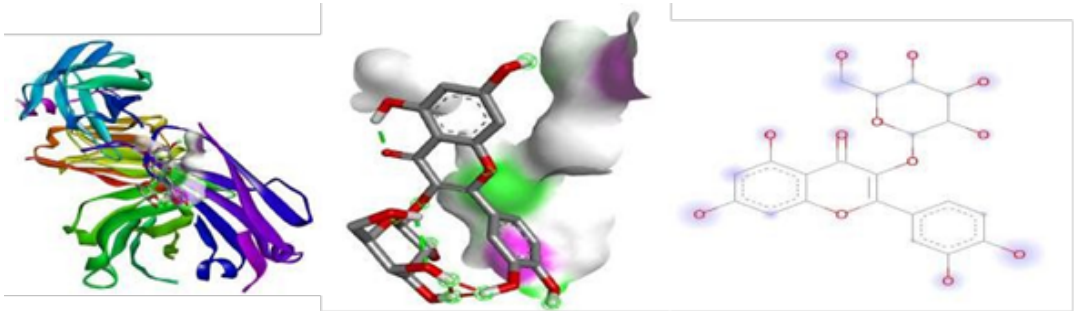


Fig. 10: 3D and 2D Molecular docking of compound 5H3M1P1C4O with 7RPU protein

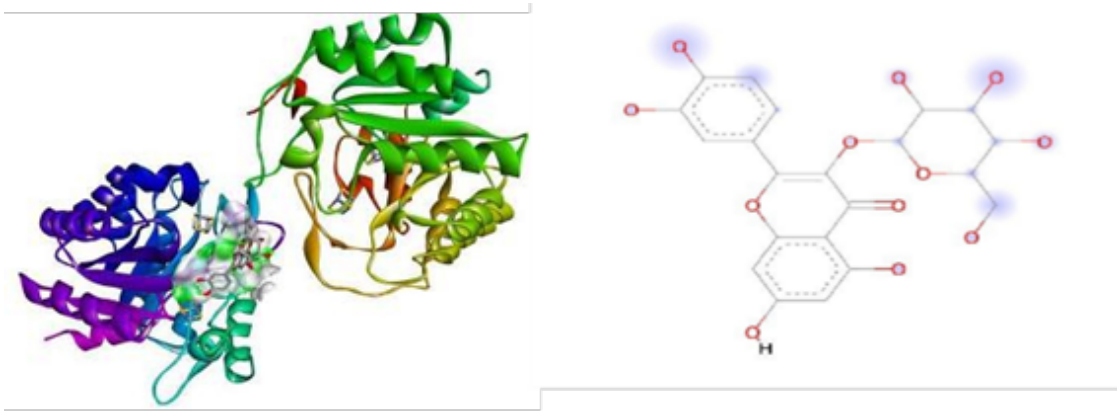


Fig. 11: 3D and 2D Molecular docking of compound 5H3M1P1C4O with 8TSK protein

charge transfer towards the antibonding C–H orbital. Notable $\sigma \rightarrow \pi^*$ interactions are also evident. The σ(O12–H53) $\rightarrow \pi^*$(C32–C33) and σ(O12–C33) $\rightarrow \pi^*$(C32–C33) interactions yield stabilization energies of 442.73 and 438.64 kcal/mol, respectively, demonstrating effective conjugative interaction between oxygen containing vbonds and the adjacent π system.

Additional $\sigma \rightarrow \sigma^*$ interactions, such as σ(O12–H53) $\rightarrow \sigma^*$(C16–H37) and σ(O12–C33) $\rightarrow \sigma^*$(C16–H37), show stabilization energies of 417.23 and 263.50 kcal/mol, confirming the portant role of oxygen-centered bonds in electron redistribution. Lone pair participation is also significant; LP(1)O12 $\rightarrow \sigma^*$(C16–H37) and LP(1)O12 $\rightarrow \pi^*$(C32–C33) interactions exhibit stabilization energies of 259.50 and 200.51 kcal/mol, respectively. Similarly, LP(1) O11 $\rightarrow \sigma^*$(C27–H46) contributes 134.87 kcal/mol, further supporting lone-pair-assisted delocalization.

$\pi^* \rightarrow \pi^*$ interactions also facilitate electron delocalization within the conjugated framework. The π^*(O8–C21) $\rightarrow \pi^*$(C19–C20) and π^*(C26–C30) π^*(C22–C23) interactions provide stabilization energies of 190.94 and 160.67 kcal/mol, respectively, confirming effective π-electron communication across the molecular skeleton.

Overall, the stabilization energies associated with $\nu \rightarrow \sigma^*$, $\sigma \rightarrow \pi*$, LP $\rightarrow \sigma^*$, LP $\rightarrow \pi^*$, and $\pi^* \rightarrow \pi^*$ interactions clearly demonstrate pronounced intramolecular charge transfer and hyperconjugative effects. The prominent involvement of oxygen-centered σ bonds and lone pair orbitals highlights their crucial role in modulating the electronic distribution and structural stability of the molecule. The electron density distribution in the occupied bonding orbitals was further examined through NBO hybrid orbital analysis. The percentage contributions of electron density over the bonded atoms, along with their s and p characters, are summarized in Table 5. The ν(O1–C16) and ν(O1–C17) bonding orbitals exhibit strong polarization towards the oxygen atom, with electron density contributions of 68.29% and 67.31%, respectively, while the corresponding carbon atoms contribute 31.71% and 32.69%. The hybridization of oxygen in these bonds corresponds to sp^{2}\58 and sp^{2}\51, with dominant p-character (72.06% and 71.48%), indicating directional bonding and enhanced electronegativity of oxygen.

In contrast, the σ(C32–H49) bond shows higher electron density localization on the carbon atom (60.52%) compared to hydrogen (39.48%). The carbon atom in this bond exhibits sp^{2}\48 hybridization with a predominant p-character (71.24%), whereas hydrogen contributes almost pure s-character (99.95%), as expected. The observed polarization of σ-bonds toward oxygen atoms confirmed that electron density was preferentially accumulated around oxygen, making it the principal electron-rich centre. This uneven charge distribution around oxygen atoms significantly influences the molecular polarity and contributes to the overall electronic behaviour of the molecule.

Investigation of UV–Visible absorption characteristics

The UV–Visible absorption behaviour of 5H3M1P1C4O was investigated experimentally and theoretically to elucidate its electronic excitation characteristics in different media (Fig. 5 and Table 6). Experimentally, the compound exhibits absorption maxima at 330 nm in the gas phase, 350 nm in methanol, and 360 nm in ethanol, corresponding to optical band gap energies of 3.76 eV, 3.54 eV and 3.44 eV, respectively, indicating a clear bathochromic shift with increasing solvent polarity. Time-dependent DFT calculations reproduce this trend well and predict dominant absorption bands at 357.35 nm (27983 cm^{-1}) in the gas phase, 358.42 nm (27900 cm^{-1}) in methanol, and 358.42 nm (27900 cm^{-1}) in ethanol, which are primarily associated with HOMO $\rightarrow$ LUMO transitions contributing more than 92–93%, confirming the $\pi \rightarrow \pi^*$ nature of the excitation. Additional higher-energy transitions were observed around 317–328 nm and 300–308 nm, arising mainly from HOMO $\rightarrow$ LUMO and orbital contributions such as H-5, H-3, H-2, and H-6 to LUMO, with varying percentages depending on the medium. The oscillator strength values indicate enhanced transition probability in polar solvents, with the highest intensity observed in methanol (f = 0.3775), reflecting improved stabilization of the excited state. All computed transitions correspond to allowed singlet–singlet (singlet-A) excitations. The gradual reduction in band gap from gas to alcoholic solvents confirms solvent-induced electronic delocalization and stabilization of the excited states in 5H3M1P1C4O, leading to good agreement between experimental observations and theoretical predictions.

Topological analysis (ELF and LOL)

Electron localization within the molecular framework of 5H3M1P1C4O was examined using the electron localization function (ELF) and the localized orbital locator (LOL), both of which are effective descriptors for understanding bonding characteristics and electron pairing behaviour. The ELF primarily highlights regions associated with covalent bonding and lone-pair electrons, while the LOL emphasizes areas of maximum orbital localization derived from kinetic energy density. As a result, ELF and LOL analyses are complementary and provide consistent insight into the electronic structure of the molecule. The two-dimensional ELF and LOL colour-filled maps along with their corresponding contour plots are illustrated in Figures 6 (a,b) and 6 (c,d). In both representations, regions of high electron localization are indicated by red colour, whereas blue regions correspond to low electron localization. Intermediate localization zones are shown by green-to-yellow shades.

From the ELF maps, strong electron localization is clearly observed around the hydrogen atoms and in the vicinity of ν-bond regions, indicating pronounced Pauli repulsion between electrons of identical spin. These regions appear as intense red patches, confirming the presence of localized bonding interactions. In contrast, comparatively lower ELF values (blue regions) are distributed around selected carbon and oxygen atoms within the heterocyclic and aromatic framework, reflecting reduced electron localization in these regions.

The LOL plots further support these observations. High LOL values, represented by red contours, are predominantly associated with non-bonding and localized valence regions, particularly around hydrogen atoms and specific bonding domains. Regions close to the inner valence shells, where electron density is relatively depleted, display lower LOL values and appear in blue. This distribution indicates that while the molecule contains localized bonding domains, extended delocalization is limited within the core framework.

Overall, the combined ELF and LOL analyses confirm that 5H3M1P1C4O exhibits distinct localized electron density around hydrogen atoms and selected bonding regions, along with comparatively weaker localization near certain carbon and oxygen centres. This electron distribution pattern reflects the balance between localized covalent interactions and regions of lower electron concentration within the molecular structure.

Fukui function analysis and dual reactivity descriptors

The Fukui function, which is derived from Mulliken population analysis and used within the density functional theory framework, provides a good description of the electrophilic and nucleophilic properties of specific atomic sites. By characterizing a molecule's electron acceptivity or electron donation, the Fukui indices quantify its chemical reactivity and selectivity.

Hence, fr– corresponds to the electrophilic attack index, and fr+ represents the nucleophilic attack index in the Fukui function. Positive values suggest nucleophilic character, and negative values signal electrophilic nature, which is further made easier to identify reactive sites by dual descriptor νfr. Table 7 displays the molecule's computed dual descriptor values and decreased Fukui functions. Amino acid 21C has the highest negative value (-0.071) in the data, suggesting that it is the electrophilic site in the molecule. Alternatively, the most strongly nucleophilic behavior is shown by the greatest positive value (0.034) for atom 24C. O7 and O8 are just a couple of the oxygen atoms; C13, C17, C20, C21, C25, C27, C28, C30, C32 and C33 are a bunch of carbon atoms; and numerous hydrogen atoms are electrophilic centers because they have negative values. However, some hydrogen atoms and atoms such as O1, O2, O3, O4, O5, O6, O9, O10, O11, O12, C14, C15, C19, C22, C24, C26, C29 and C31 show positive νfr values, suggesting that they have nucleophilic potential. The existence of electrophilic and nucleophilic areas gives credence to the molecule's strong chemical reactivity and implies that it can effectively interact with biological systems.

Hyperpolarizability investigations

Nonlinear optics (NLO) deals with phenomena that arise from the nonlinear interaction between electromagnetic radiation and matter, particularly when intense light propagates through an optical medium. In recent years, the development of molecular systems exhibiting enhanced NLO

responses has attracted considerable attention because of their wide-ranging applications in optical switching, signal modulation, data storage and telecommunication technologies. Materials possessing strong nonlinear responses enable efficient manipulation of light, thereby extending the functional limits of modern optical science[27].

From a theoretical perspective, molecular polarizability and hyperpolarizability parameters obtained through quantum chemical calculations are often found to correlate well with experimental observations. Consequently, comparison of the calculated NLO parameters with those of a standard reference material such as urea provides a reliable measure for assessing the NLO efficiency of newly designed molecules[28].

Table 8 summarizes the calculated nonlinear optical properties of 5H3M1P1C4O in the gas phase, which include the dipole moment (μ), average polarizability (α), polarizability anisotropy ($\Delta\alpha$), and first-order hyperpolarizability (β). Confirming the presence of charge asymmetry within the molecule and demonstrating favorable dipolar properties necessary for nonlinear optical activity, the optimized structure displays a non-zero dipole moment (μ = 3.56 D)[29]. The significant anisotropy of polarizability ($\Delta\alpha = 6.214 \times 10^{-23}$ esu) indicates that the electronic reaction is direction-dependent, while the computed mean polarizability value ($\alpha = 3.969 \times 10^{-23}$ esu) shows how easily the electron cloud may be warped by an external electric field. It is worth noting that the title molecule has a substantially higher total first-order hyperpolarizability ($\beta = 1.643 \times 10^{-29}$ esu) than urea, a regularly used benchmark NLO material. The molecular framework's efficient intramolecular charge transfer, robust donor-acceptor contacts, and prolonged π-conjugation are the reasons for this improvement[30].

In addition to global NLO parameters, local reactivity descriptors derived from Mulliken atomic charges and Fukui functions (Table 7) provide deeper insight into the charge-transfer behavior governing the nonlinear response. The oxygen atoms exhibit comparatively larger negative charges and notable values of local softness, indicating their dominant role as electron-rich centers. Conversely, several carbon and hydrogen atoms display positive Fukui function values for electrophilic attack, highlighting potential charge migration pathways within the molecule. The dual descriptor analysis further confirms the coexistence of electrophilic and nucleophilic regions, reinforcing the push–pull electronic nature of the compound[31].

Overall, the combined analysis of hyperpolarizability parameters and local softness descriptors clearly demonstrates that 5H3M1P1C4O possesses strong nonlinear optical characteristics. These findings establish the title compound as a promising candidate for future NLO applications and suggest its potential relevance in optoelectronic and medicinal chemistry domains where charge-transfer interactions play a crucial role[32].

Integrated RDG analysis and structural stability

Using Reduced Density Gradient (RDG) analysis, which allows the visualization of non-covalent interactions (NCIs) based on electron density and its derivatives, the structural stability and conformational landscape of 5H3M1P1C4O were assessed[33-34]. Figure 7 shows the RDG scatter plot, which divides the interaction regimes into three regions: the blue region represents strong attractive interactions, the green region represents Van der Waals forces, and the red region represents steric repulsion. The presence of strong intramolecular hydrogen bonding that supports the structural integrity of the molecule is indicated by the prominent blue spikes, which show that attractive stabilizing forces are dominant[35]. These results are in good agreement with the experimental Raman spectra, which show that the localized strength of these H-bond networks is reflected by the high-frequency hydroxyl stretching modes (3200-3850 cm^{-1}) with large potential energy distribution (PED) values. Steric repulsion ($\lambda 2)\nu > 0$) inside the aromatic rings and sugar moiety is crucial in defining the final 3D conformation, and the presence of dispersive Van der Waals interactions ($\lambda 2)\nu = 0$) enhances binding efficiency in addition to these stronger forces [36,37].

Pharmaceutical analysis of 5H3M1P1C4O

The oral bioavailability of the studied compound 5H3M1P1C4O was evaluated using Swiss ADME-predicted physicochemical, pharmacokinetic, and drug-likeness parameters, as summarized in Table 9. The compound exhibits a molecular weight of 464.38 g/mol and contains four rotatable bonds, both of which fall within the acceptable limits for

orally administered drug candidates. Although the compound shows a relatively high number of hydrogen bond donors (8) and acceptors (12), it demonstrates favorable aqueous solubility across multiple predictive models (Log S_ESOL = –3.04; Log S_SILICOS-IT = –1.51), ensuring effective dissolution in the gastrointestinal environment. The consensus lipophilicity value (log P = –0.38) indicates a hydrophilic character that supports solubility while minimizing nonspecific tissue accumulation[38-39].

The elevated topological polar surface area (TPSA = 210.51 Å²) accounts for the predicted low gastrointestinal absorption and the absence of blood–brain barrier permeation. Importantly, the compound is not predicted to be a P-glycoprotein substrate and does not inhibit major cytochrome P450 isoforms, suggesting a low risk of efflux-mediated transport and metabolic drug–drug interactions. The physicochemical and pharmacokinetic properties listed in Table 9 comply with the acceptable criteria for orally active drug candidates, with a predicted bioavailability score of 0.17. These results suggest that 5H3M1P1C4O is a potential candidate for further development as an oral therapeutic agent[40-41].

Molecular docking analysis of 5H3M1P1C4O with four selected protein targets

The molecular docking performance of the ligand 5H3M1P1C4O against the four target proteins was comparatively evaluated using binding energy and interaction distance as the primary criteria. The quantitative docking parameters are summarized in Table 10 and Table 11, while the corresponding three-dimensional and two-dimensional binding conformations are illustrated in Fig. 8–11.

Table 10 summarizes the docking scores and matching binding parameters that were computed. Results showing negative binding energies for all four proteins show that the ligand interacts favourably inside their active regions. The binding energy of the ligand was –5.23 kcal/mol for 7RPU, –4.29 kcal/mol for 3ERT, –4.25 kcal/mol for 6J90 and –3.67 kcal/mol for 8TSK, out of all the targets that were studied. Distinct structural contexts and amino acid compositions of binding pockets among proteins account for the detected fluctuations in binding energy.

The protein-ligand interactions are examined in depth in Table 11, which lists the important amino acid residues that bind and the kind of interactions between them. Depending on the protein target, the ligand might establish electrostatic contacts, hydrophobic alkyl interactions, π-alkyl, carbon-hydrogen, and traditional hydrogen bonds as stabilizing interactions. These linked residues are essential for docked complex stability and for attaching the ligand to the active site.

Hydrogen bonding interactions were found to be particularly important in stabilizing the ligand within the binding cavity, while hydrophobic interactions further enhanced binding strength by promoting favourable van der Waals contacts. The presence of multiple interaction types suggests that the ligand is well accommodated within the active-site regions of the studied proteins. Overall, the docking results summarized in Tables 10 and 11 demonstrate that 5H3M1P1C4O exhibits a stable and energetically favourable binding profile, with 7RPU showing the most promising interaction characteristics among the evaluated targets.

CONCLUSION

The integrated molecular docking and density functional theory analyses provide mechanistic insight into the interaction profile of 5H3M1P1C4O with selected cancer-related protein targets. The investigated proteins represent key molecular systems involved in cancer- associated pathways, rather than being linked to a single cancer type. This approach enables evaluation of the general anticancer potential of the compound across diverse biological targets[42-43].

Comparative docking analysis revealed noticeable differences in binding affinity and interaction patterns among the four protein structures. One target protein exhibited the most favorable binding energy, indicating stronger ligand–protein complex stability compared with the remaining proteins. This enhanced affinity can be attributed to the efficient accommodation of 5H3M1P1C4O within the active site, supported by a combination of π–π stacking, π–alkyl, hydrophobic and van der Waals interactions involving key amino acid residues lining the binding pocket[43-45].

Proteins displaying less favourable docking

scores showed comparatively weaker interaction networks, characterized by reduced hydrophobic complementarity and fewer stabilizing non- covalent contacts. These findings suggest that the anticancer activity of 5H3M1P1C4O is strongly influenced by binding site geometry, residue composition, and electronic compatibility, rather than disease specificity[45-46].

From a structure-based design perspective, the aromatic and heterocyclic architecture of 5H3M1P1C4O plays a critical role in mediating hydrophobic and π-electron interactions, while limited hydrogen bonding contributes to positional stabilization. These features collectively highlight the importance of molecular planarity and electronic distribution in achieving favorable protein binding[46-47].

Complementary DFT calculations further support the docking results by revealing delocalized electron density across the chromen-4-one framework, facilitating π-mediated interactions with aromatic residues of the proteins. The calculated HOMO–LUMO energy gap indicates adequate chemical stability combined with sufficient reactivity to support non-covalent binding. In addition, the frontier molecular orbital distribution identifies potential sites for rational functional modification aimed at enhancing interaction strength and target selectivity[48].

Declarations Funding

No external financial support was received for conducting this research.

Conflicts of Interest

The authors state that there are no conflicts of interest related to this work.

Data Availability

All data generated or analyzed during this study are included in this article and its supplementary information.

Ethics Approval

Not applicable, as this study did not involve human participants or experimental animals.

ACKNOWLEDGEMENTS

The authors would like to state that there are no acknowledgements related to this work.

Author Contributions

Thangavelan Niruban Balu: Investigation, formal analysis, and preparation of the original draft. Dr. P. Venkatesh: Supervision and guidance of the research work.

Rajakumari Subramaniyan: Concept development, manuscript review and editing, data curation, and visualization.

REFERENCES

1. World Health Organization. WHO Report, 2024.
2. International Agency for Research on Cancer. IARC, 2024.
3. Kilmister, E. J. Review Article, 2023.
4. Lim, Z. F.; Ma, P. C. *Journal of Hematology & Oncology,* **2019**, *12*, , 134-150. https://doi.org/10.1186/s13045-019-0813-0
5. Khan, S. U. *Cancer Drug Resistance*, **2022**, *5*, 23-145. https://doi.org/10.20517/cdr.2022.12
6. Jain, A. *Cancers*, **2021**, *13*, 425. https://doi.org/10.3390/cancers13030425
7. Al-Karmalawy, A. A. *Molecules*, **2021**, *26*, 518. https://doi.org/10.3390/molecules26020518
8. Meng, X. Y.; Zhang, H. X.; Mezei, M.; Cui, M. *Current Computer-Aided Drug Design,* **2011**, *7*, 46-157. https://doi.org/10.2174/157340911795677602
9. Agu, P. C. *Scientific Reports,* **2023**, *13*,13398. https://doi.org/10.1038/s41598-023-39921-3
10. Magaji, B. *Journal of Molecular Modeling*, **2024**, *30*, 145. https://doi.org/10.1007/s00894-024-05521-0
11. Paneru, T. R. *Journal of Molecular Structure,* **2024**, *1290*, 136-145. https://doi.org/10.1016/j.molstruc.2024.136145
12. El-Shamy, N. T. *Molecules,* **2022**, *27*, 620. https://doi.org/10.3390/molecules27030620
13. Mellaoui, M. D. *Journal of Molecular Structure,* **2024**, *1295*, 137210. https://doi.org/10.1016/j.molstruc.2024.137210

14. Morris, G. M.; Huey, R.; Lindstrom, W.; Olson, A. J. *Journal of Computational Chemistry,* **2009**, *30*, 2785-2791. https://doi.org/10.1002/jcc.21256
15. RCSB Protein Data Bank. Protein Data Bank, 2024, 3ERT. https://doi.org/10.2210/pdb3ert/pdb
16. NCBI Structure Database. MMDB, 2024,3ERT.
17. Morris, G. M.; Huey, R.; Lindstrom, W.; Olson, A. J. *Journal of Computational Chemistry*, **2009**, *30*, 2785-2791. https://doi.org/10.1002/jcc.21256
18. Scripps Research Institute. User Guide, **2023**.
19. Jebapriya, J. C.; Raj, R.; Kumar, S. *Materials Today: Proceedings,* **2022,** *62*, 2100- 2107. https://doi.org/10.1016/j.matpr.2022.02.210
20. Potla, K. M. *Vibrational Spectroscopy*, **2023**, *124*, 103456. https://doi.org/10.1016/j.vibspec.2023.103456
21. Govindammal, M.; Saravanan, R.; Kumar, V. *Heliyon*, **2020**, *6*, e03912. https://doi.org/10.1016/j.heliyon.2020.e03912
22. Saral, A.; Kumar, S.; Devi, R. *Heliyon*, **2024***, 10,* e24011. https://doi.org/10.1016/j.heliyon.2024.e24011
23. Edwin, B.; Joseph, P.; Thomas, K. *Vibrational Spectroscopy*, **2012**, *60*, 150-156. https://doi.org/10.1016/j.vibspec.2012.02.005
24. Herzberg, G. *Van Nostrand,* **1950**.
25. Jamróz, M. H. *Vibrational Spectroscopy,* **2013**, *114*, 1-15. https://doi.org/10.1016/j.vibspec.2013.04.002
26. Çırak, Ç.; Karabacak, M.; Kurt, M. *Vibrational Spectroscopy,* **2011**, *57*, 123-130. https://doi.org/10.1016/j.vibspec.2011.05.003
27. Çırak, Ç.; Karabacak, M.; Kurt, M. *Journal of Molecular Structure*, **2012**, *1012*, 1-8. https://doi.org/10.1016/j.molstruc.2011.12.021
28. Suvitha, A.; Kumar, P.; Devi, L. *Spectrochimica Acta* Part A, **2014**, *120*, 1-7. https://doi.org/10.1016/j.saa.2013.09.012
29. Dai, F.; Liu, Y.; Zhang, H. *Fuel,* **2023**, *332*, 125133. https://doi.org/10.1016/j.fuel. 2022.125133
30. OpenStax. LibreTexts, **2024**.
31. Tsioptsias, C.; Pavlidou, E.; Panayiotou, C. *Journal of Molecular Structure*, **2022**, *1267*, 133614. https://doi.org/10.1016/j.molstruc.2022.133614
32. Malaganvi, S. S.; Patil, P.; Kumar, R. *Journal of Molecular Structure*, **2019**, *1195*, 1-9. https://doi.org/10.1016/j.molstruc.2019.05.021
33. Boyd, R. W. Academic Press, **2020**.
34. Prasad, P. N.; Williams, D. J. Wiley, **1991**.
35. Zyss, J.; Ledoux, I. Chemical Reviews, **1994**, *94*, 77-105. https://doi.org/10.1021/cr00025a003
36. Janani, J.; Kumar, S.; Devi, R. *Journal of Molecular Modeling,* **2023**, *29*, 210. https://doi.org/10.1007/s00894-023-05521-3
37. Kumar, S.; Patel, R.; Singh, *V. Optical Materials*, **2023**, *140*, 113921. https://doi.org/10.1016/j.optmat.2023.113921
38. Geerlings, P.; De Proft, F.; Langenaeker, W. *Chemical Reviews*, **2003**, *103*, 1793-1874. https://doi.org/10.1021/cr990029p
39. Chakraborty, D.; Chattaraj, P. K. *Chemical Science*, **2021**, *12*, 6264-6279. https://doi.org/10.1039/D1SC01234A
40. Johnson, E. R.; Keinan, S.; Mori-Sánchez, P.; Contreras-García, J.; Cohen, A. J.; Yang, W. *Journal of the American Chemical Society*, **2010**, *132*, 6498-6506. https://doi.org/10.1021/ja100936w
41. Johnson, E. R. *Manual,* 2023.
42. ChemTools Development Team. Documentation, **2023**.
43. LibreTexts, **2024**.
44. Tsioptsias, C. *Journal of Molecular Structure,* **2022**, *1267*, 133614.
45. Daina, A.; Michielin, O.; Zoete, V. *Scientific Reports*, **2017**, *7*, 42717. https://doi.org/10.1038/srep42717
46. SwissADME Web Tool, **2024**.
47. Veber, D. F.; Johnson, S. R.; Cheng, H. Y.; Smith, B. R.; Ward, K. W.; Kopple, K. D. *Journal of Medicinal Chemistry,* **2002**, *45*, 2615-2623. https://doi.org/10.1021/jm020017n
48. Stegemann, S.; Leveiller, F.; Franchi, D. *Drug Discovery Today*, **2023**, *28*, 103456. https://